Inertial focusing of microparticles, bacteria and blood in serpentine glass channels

Pablo Rodriguez-Mateos,[1] Bongkot Ngamsom,[1] Charlotte E. Dyer,[2] Alexander Iles,[1] Nicole Pamme[1*]

[1] Department of Chemistry and Biochemistry, University of Hull, UK.

[2] Department of Biomedical Sciences, University of Hull, UK.

*Correspondence should be addressed to the following author(s):

Prof. Nicole Pamme

Department of Chemistry and Biochemistry, Faculty of Science and Engineering

University of Hull

Cottingham Road, Hull, HU6 7RX, UK

n.pamme@hull.ac.uk

Abstract

Early detection of pathogenic microorganisms is pivotal to diagnosis and prevention of health and safety crises. Standard methods for pathogen detection often rely on lengthy culturing procedures, confirmed by biochemical assays, leading to >24 h for a diagnosis. The main challenge for pathogen detection is their low concentration within complex matrices. Detection of blood-borne pathogens via techniques such as PCR requires an initial positive blood culture and removal of inhibitory blood components, reducing its potential as a diagnostic tool. Amongst different label-free microfluidic techniques, inertial focusing in microscale channels holds great promise for automation, parallelization and passive continuous separation of particles and cells. This work presents inertial microfluidic manipulation of small particles and cells (1-10 µm) in curved serpentine glass channels etched at different depths (deep and shallow designs) that can be exploited for (1) bacteria pre-concentration from biological samples and (2) bacteria-blood cell separation. In our shallow device, the ability to focus *Escherichia coli* (*E. coli*) into the channel side streams with high recovery (89% at 2.2x pre-concentration factor) could be applied for bacteria pre-concentration in urine for diagnosis of urinary tract infections. Relying on differential equilibrium positions of red blood cells (RBCs) and *E. coli* inside the deep device, 97% RBCs were depleted from 1:50 diluted blood with 54% *E. coli* recovered at a throughput of 0.7 mL min^{-1}. Parallelization of such devices could process relevant volumes of 7 mL whole blood in 10 min, allowing faster sample preparation for downstream molecular diagnostics of bacteria present in bloodstream.

1 Introduction

Surveillance is the first step in limiting diseases caused by pathogenic microorganisms, and their early detection is crucial for diagnosing and preventing crises related to health, safety and wellbeing [1]. Pathogen detection is often hampered by low concentrations present in complex matrices such as food and body fluids and, as a result, additional pre-concentration and separation steps are usually required prior to analysis [2,3]. For example, in bacteremia, pathogen burden can be as low as 10 – 100 per mL, whilst the host cell background is vastly higher (10^9 blood cells mL^{-1}) [4-6]. Although molecular diagnostics hold the potential to greatly enhance

pathogen analysis and identification, standard methods for pathogen detection still rely heavily on traditional lengthy culture techniques to isolate and enumerate viable cells in samples, followed by confirmation using biochemical or serological tests. In blood stream infections, techniques such as PCR, fluorescence *in situ* hybridization and mass spectroscopy require an initial positive blood culture, resulting in 18 to 24 h for a diagnosis [6]. In addition, removal of blood components that interfere with PCR amplification is necessary [7].

Conventional methods employing macroscale instruments for label-free cell separation are centrifugation and mechanical filtration [6,8]. Although simple to operate and successful in separating blood components, centrifugation can lead to contamination of sorted levels during extraction and may cause lysing of blood cells and poor bacteria recovery [6,9]. Mechanical filtration is prone to clogging during continuous operation. It also proves challenging with deformable cells such as RBCs, as these can squeeze through membrane pores that are smaller than their size, especially when used in screening of bacteria in blood [6,8].

Various label-free microfluidic separation platforms have been developed using acoustic, magnetic, electric, and optical forces [10-12]. In contrast, inertial microfluidics utilizes simple microscale channel geometries and fluid pressure driven flows to accomplish effective and precise control for particle/cell manipulation without additional force fields [13-16]. Some of the broader advantages are its high throughput, predictability, and potential for automation, parallelization and passive continuous separation of particles and cells [17,18]. In addition, several studies have reported cell viability not being significantly affected by the high flow and shear rates often used in inertial microfluidic systems [19-24]. This is presumably because cells are not stationary on a surface, but move and rotate with the fluid without significant deformation [25].

Microfluidic channels with different types of straight and curving geometries have been employed for inertial particle and cell focusing, including stepped/expanding channels [8,26-28], spirals [19-21,29-44], single curves [45-48], symmetric and asymmetric serpentine curves [22-24,49-56] and combinations of spiral with asymmetric serpentine curves [57]. Although spiral devices are the most common type of curved geometry employed, a major drawback from spiral and single curved channels that only turn in one direction is the difficulty of arranging many of them in parallel on a

3

82 single substrate [58]. Serpentine curved channels with alternating directions are more
83 easily parallelized, require less linear distance than straight ones, and by introducing
84 asymmetry in the curvature can achieve similar focusing to spirals [25]. Different
85 designs of serpentine devices have been used for focusing different microparticle
86 sizes (2-20 µm) [23,54], separating multiple blood components [23,53,56,59],
87 pathogenic microorganisms from blood [5,8,60-63], various types of rare cancer cells
88 [51,55,64-66], neurons [24] and pre-concentrating cyanobacteria [49].

89 In this communication, we investigated for the first time curved serpentine channels
90 etched in glass for inertial focusing of small particles and cells (1-10 µm). Two
91 distinctive focusing behaviors from the two etched depths were explored for their
92 potential uses for (i) pathogen pre-concentration, and (ii) separation of pathogenic
93 bacteria from blood.

2 Theory

95 In microfluidic fluid flow, the relative ratio between inertial and viscous effects in a
96 channel is represented by the dimensionless channel Reynolds number (Re_c) [67]:

$$Re_c = \frac{\rho U D_h}{\mu} \tag{1}$$

98 where ρ is the density of the fluid (kg m^{-3}), U is the average flow velocity of the flowing
99 liquid (m s^{-1}), D_h is the hydraulic diameter of the channel (m) calculated as D_h =
100 $2wd/(w+d)$ for a rectangular cross-section (w and d being the width and depth of the
101 channel) and μ is the fluid viscosity (Ns m^{-2}). Inertial microfluidics works in an
102 intermediate range (~1 < Re_c < ~100) between Stokes regime ($Re_c \rightarrow 0$) and turbulent
103 regime (Re_c ~2000) [15].

104 Taking into account the particle diameter a (m), the particle Reynolds number (Re_p)
105 can be defined to describe the flow of particles in closed channel systems [22,68]:

$$Re_p = \frac{\rho U a^2}{\mu D_h} \tag{2}$$

107 Particles suspended in fluids are subjected to hydrodynamic drag and lift forces that
108 are strongly influenced by the fluid dynamic parameters of the system [25,69]. In
109 serpentine channels, two main forces take place: (1) inertial lift and (2) drag forces.
110 Inertial lift forces can be subdivided into the shear gradient lift force (pushing particles

away from the channel centerline) and the wall-effect lift force (pushing the particles away from the channel wall towards the center). The interaction between these two forces is the net lift force (F_L), which directs the particle towards a stable equilibrium position within the cross section of the microchannel (Figure 1A). This phenomenon is known as 'inertial particle migration'. The net lift force can be expressed as [70]:

$$F_L = \frac{\rho U^2 a^4}{D_h^2} f_c \qquad (1)$$

where f_c is a lift coefficient. This equation illustrates specifically the very strong dependence of lift force on particle diameter, to the fourth order. Because of this dependence on a, focusing smaller particles in a given geometry requires much higher flow velocity (U) and a reduced microchannel cross-sectional area (D_h) than for larger particles or cells.

In a straight channel with square cross-section, particles migrate towards the midpoint of one of the edges of the wall, generating four equilibrium positions. In a straight channel with rectangular cross-section, the equilibrium positions reduce to two, focusing near the midpoints on the wider faces of the channels (Figure 1B) [68,71,72].

Drag forces are produced by a secondary flow (Dean flow), which arises when microscale channels curve or become asymmetric [15,23,68]. Particles in the center move outwards and circulate back around the channel edges creating two symmetric and counterrotating vortices perpendicular to the primary flow direction (Figure 1C). The drag force (F_D) scales as $F_D \sim \rho U^2 a D_h^2 / r$, where r is the radius of curvature of the channel. Two dimensionless numbers that characterize this secondary flow are the curvature ratio ($D_h / 2r$) and Dean number ($De = Re_c \sqrt{\delta}$), based on the flow velocity in the channel [25].

The competition between the net inertial lift and drag force can be used to manipulate the focusing profile of particles and reduce the number of equilibrium positions. The ratio between inertial lift and drag forces is the inertial force ratio (R_f) [25]:

$$R_f = \frac{a^2 R}{H^3} \qquad (5)$$

where R is the largest radius of curvature (m) in the system and H is the smallest dimension of the channel (m). To observe focusing, Di Carlo reported $R_f > 0.04$. For a large R_f value, the inertial lift force dominates the Dean drag force, whilst for a small

141   R_f value the secondary flow effect is dominant. R_f is a strong function of the particle

142   size; as a result, when two different particles are introduced, they can be separated

143   based on their different equilibrium positions.

144   In addition, the ratio of inertial-lift force and the Dean-drag force (F_L/F_D) was expressed

145   as a dimensionless number (δ), taking into account the relationships of the channel

146   curvature ratio ($D_h/2r$), channel aspect ratio (d/w), particle-blockage ratio (a/D_h), and

147   Dean number (De) [13,73]:

148

$$\delta = \frac{a/D_h}{De^{1/2}(D_h/2r)^{3/4}} \tag{6}$$

149   Exploiting δ and a modified particle-blockage ratio, $2(a/D_h)/(1 + d/w)$, reflecting the

150   influence of the channel aspect ratio, a recent experimental operational map was

151   constructed to predict the focusing pattern of different microparticles (5-20 μm) in

152   symmetric sinusoidal microchannels [73].
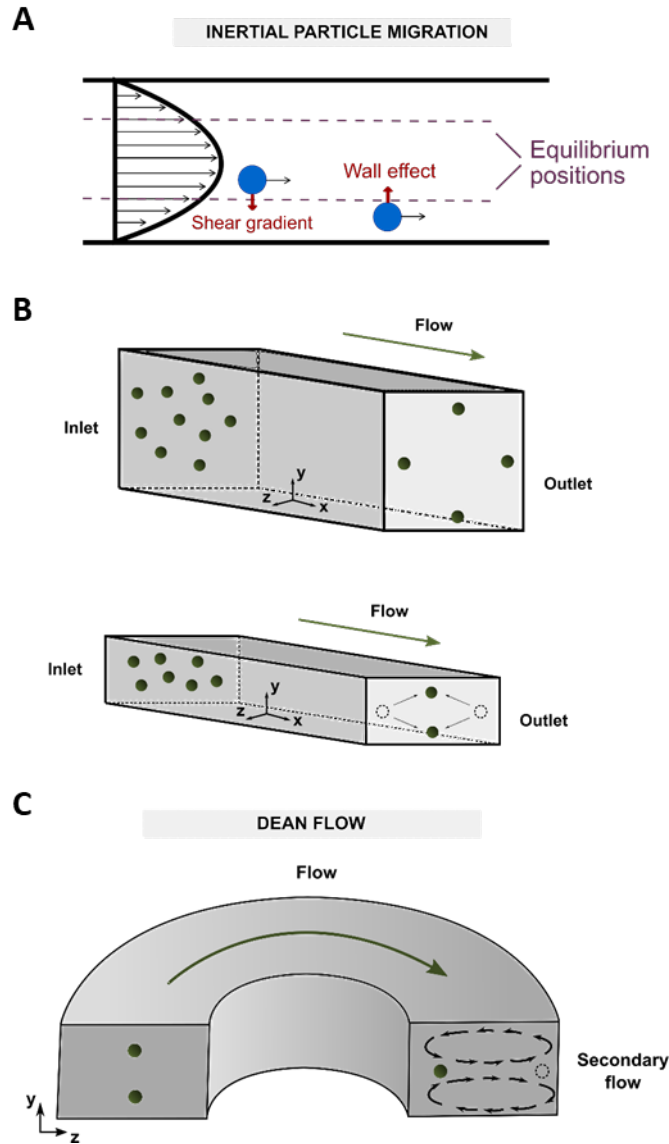
Figure 1. A) Schematic representation of both inertial lift forces perpendicular to the flow direction and responsible for the lateral migration of particles to their equilibrium positions in straight channel flows: (1) Shear-gradient lift force, directed down the shear gradient and (2) wall-effect lift force, directed away from the wall. B) In square straight channels, particles focus to four equilibrium regions centred at the faces of the channels. In rectangular straight channels, particles migrate towards the two wider faces. C) When introducing channel curvature, a secondary flow (Dean flow) creates two counter-rotating vortices (black arrows) perpendicular to the primary flow direction.

3 Materials and methods

3.1 Device design, fabrication, and interfacing

Inertial microfluidic devices were designed in AutoCAD (Figure S1, Supporting Information). Glass devices were patterned onto a 1.15 mm thick glass wafer coated with chromium and photoresist layers (Schott B270, Tellic, USA) using contact mask

lithography. After photo-development and chrome etching, the glass was wet etched with a solution of hydrofluoric acid to a depth of 25 µm or 40 µm (Figure 2A, B) [74]. Access holes were CNC drilled (Datron M7) into the etched plate, which was subsequently thermally-bonded to a Schott B270 glass cover plate [75]. The device footprint was 7.5 cm x 2.5 cm. Polytetrafluoroethylene (PTFE) Teflon tubing (1.58 mm OD x 0.5 mm ID, Supelco) was glued (Epoxy Adhesive 2014-2, Araldite) to the inlets and outlets of the device (Figure 2C) and interfaced (adapters and connectors, Kinesis) to a 2.5 mL glass syringe with fixed Luer lock (SGE). Particle/cell suspensions were introduced into the device using a syringe pump (Pump 11 Elite, Harvard Apparatus) (Figure 2D).
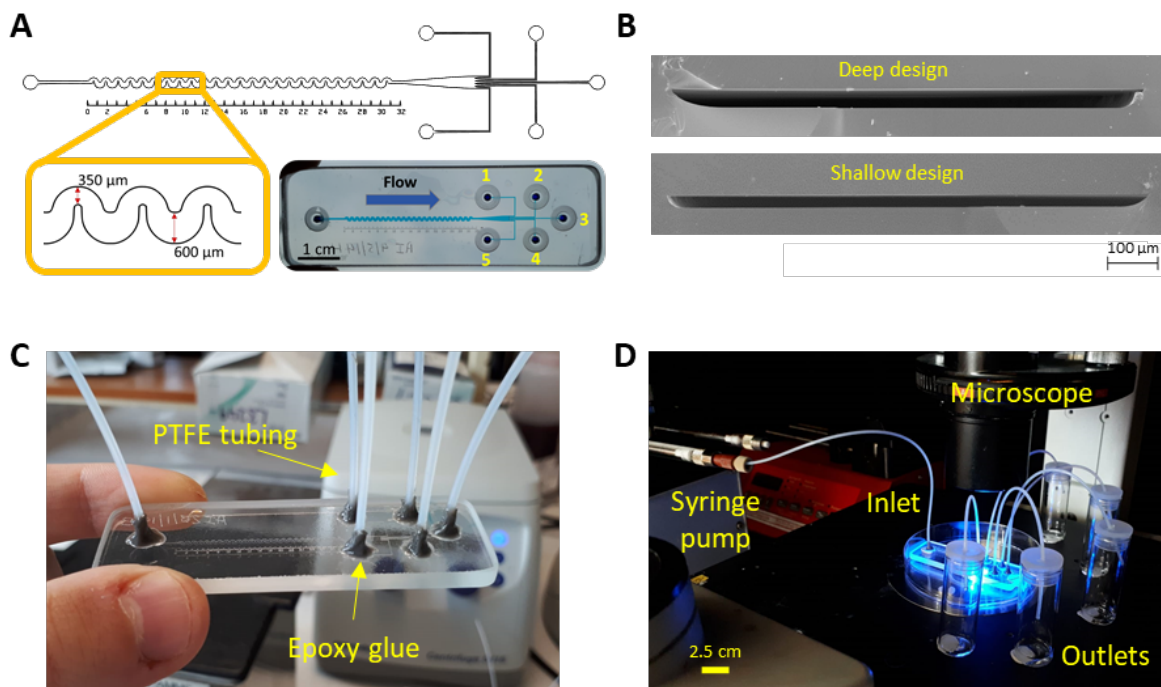
Figure 2. A) Device drawing in AutoCAD with channel width dimensions and photograph of final device filled with blue food dye solution. Solutions were pumped from the inlet (left) to the outlets (right). Outlets are numbered as a reference. B) SEM images of the channel cross-section of the two designs: deep design = 40 µm, shallow design = 25 µm. C) Glass inertial microfluidic device interfaced with tubing. D) Typical setup with a syringe pump, glass syringe, device on an inverted microscope and glass vials to collect the outlet effluents.

3.2 Particle and cell preparation

Suspensions of 10 µm and 4.5 µm yellow-green carboxylate fluorescent particles (λ excitation/emission 441/486 nm) and 1 µm polychromatic red fluorescent particles (λ excitation/emission 525/565 nm) (Fluoresbrite, Polysciences Inc) were prepared in phosphate buffered saline (PBS) and stabilized by adding 0.1% w/v Tween 20 (PBST). Defibrinated horse blood (TCS Biosciences) was prepared by appropriately diluting in

PBS. *Escherichia coli* O157:H7 (ATCC® 700728[TM]) was grown in buffered peptone water overnight at 37 °C and serially diluted to the desired concentration in PBST (0.1% w/v). Initial concentration was calculated by UV/vis absorbance at 600 nm (Biochrom Libra S11/S12 UV/vis Spectrophotometer) and plating in sorbitol MacConkey and nutrient agar plates. *E. coli* suspensions from each outlet were quantified by serially diluting and plating on sorbitol MacConkey and nutrient agars. Streams of fluorescent particles and red blood cells (RBCs) flowing through the channels of the microfluidic device were visualized using either a Nikon Eclipse TE2000-U with a Retiga-EXL CCD camera from Media Cybernetics or a Nikon Eclipse Ti inverted microscope. Microparticles and RBCs were counted with a haemocytometer (Improved Neubauer, depth 0.1 mm 1/400 mm^2, Hawksley). Separation efficiencies for each device and particle/cell size were calculated by dividing the number of particles/cells at each outlet by the sum of the particles/cells of every outlet and multiplying by 100 to give a percentage. Error bars are ± 1 SD of three repeats.

For focusing profiles, concentrations of 10^5 particles mL^{-1} were used for 10 μm and 4.5 μm particles; 10^7 particles mL^{-1} for 1 μm particles; 5×10^6 - 1×10^7 CFUs mL^{-1} for *E. coli* suspensions; and 1:10 v/v dilution for horse blood. Particles and cells were separately pumped through both devices at volumetric flow rate of 0.7 mL min^{-1}.

For separation applications, concentrations of 10^6 particles mL^{-1} were used for 10 μm particles; 10^7 particles mL^{-1} for 4.5 μm particles; 5×10^4 CFU mL^{-1} for *E. coli*; and 1:10, 1:30 and 1:50 dilutions for horse blood. Mixtures of particles and *E. coli*, and diluted blood spiked with *E. coli* were pumped only through the deep device at volumetric flow rate of 0.7 mL min^{-1}.

4 Results and discussion

4.1 Characteristics of serpentine glass devices

The glass devices in this communication were isotropically etched, resulting in 'D-shaped' cross-section microchannels (Figure S2, Supporting Information), unlike the majority of inertial focusing devices with rectangular/squared shapes fabricated from PDMS [23,51,53-56,76] or thermoset polyester [49]. Two designs were employed, etched at two different depths from the same photomask, and referred to

9

as 'shallow design' (25-µm depth) and 'deep design' (40-µm depth). The channel pathway for both devices was laid out asymmetrically, with a series of 49 alternating narrow and wide turns over a distance of 30 mm (Figure 2A). The difference in the radii of curvature between the narrow and wide turns are not as extreme as in asymmetric serpentine devices reported by Di Carlo *et al.* [22,23] (Figure S1, Table S1, Supporting Information). The aspect ratios of our devices are low (d/w = 0.05 and 0.08 for the shallow and deep designs, respectively) compared to other reported serpentine channels (≥ 0.1) [23,49,51]. Due to the 'D-shaped' cross-section of our devices, the two counter-rotating vortices in the upper and lower parts of the channel are not symmetrical as in rectangular channels. However, the asymmetry of these vortices are presumably minute in such low aspect ratio channels (w >> d). *De* are 17.5 and 15.3 for the deep and shallow devices, respectively, similar to *De* = 21.1 reported in other asymmetric serpentine devices [22,23].
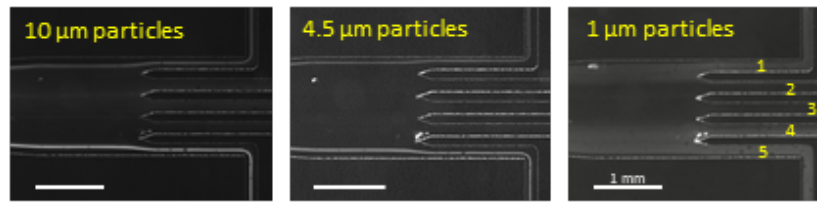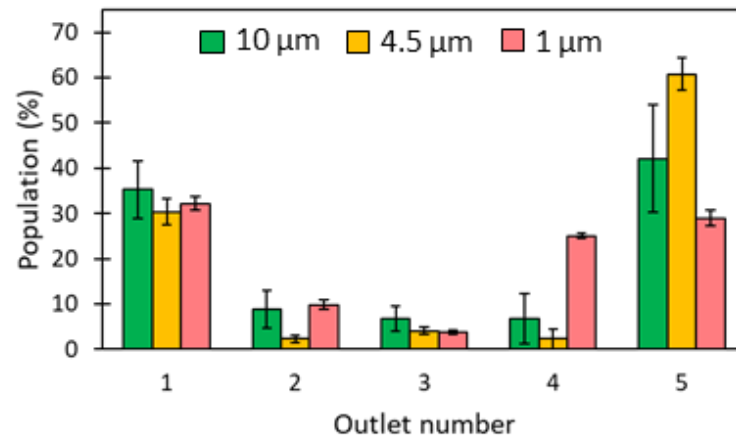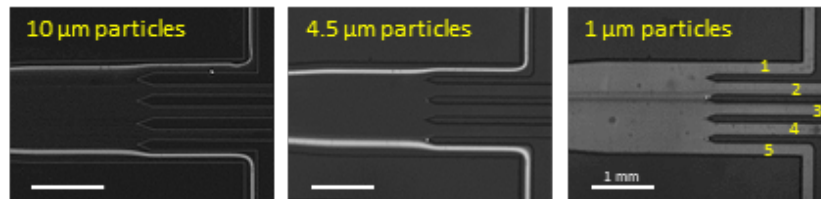
4.2 Focusing profiles of microparticles

The deep design was first assessed with rigid polystyrene particles (10 µm and 4.5 µm) at volumetric flow rates of 0.5 – 1 mL min^{-1} (Re_c = 37 – 74, Figure S3-A,B, Supporting Information). Focusing was observed along the channel edges, similarly to inertial focusing typically reported in symmetric serpentine channels where inertial lift forces dominate [22,51,56]. Reducing equilibrium positions from two to a single stream at the channel center with ≥ 8 µm-particles was reported in a symmetric serpentine device with increasing flow rates (Re_c ≥ 87) [51]. In addition, according to the experimental operational map recently reported by the same group [73], 10 µm particles in our deep device should experience one-position focusing at Re_c ≥ 74. However, no such transition was observed in our device (74 ≤ Re_c ≤ 147, results not shown here), presumably due to 3x smaller aspect ratio (d/w) of our device compared with Zhang's.

Above 0.7 mL min^{-1}, the mixing effect became predominant again with increasing flow velocities, resulting in a small migration of 4.5 µm particles into exit 4 (Figure S3-B, Supporting Information). Therefore, a fixed flow rate of 0.7 mL min^{-1} was chosen for further investigations on focusing profiles of different particles.

Suspensions of fluorescent microparticles of different sizes (10, 4.5 and 1 µm) were separately pumped through both designs at a volumetric flow rate of 0.7 mL min^{-1} (U = 91 cm s^{-1}, Re_c = 56, for the shallow design; and U = 54 cm s^{-1}, Re_c = 51, for the deep

10

design). Particle trajectories were monitored and visualized using an inverted fluorescent microscope (Figure 3). Particles of 10 µm and 4.5 µm migrated to the channel edges in both devices, exiting through outlets 1 and 5, following Zhang's experimental operational map [73] (Table S3, Supporting Information). Small particles of 1 µm focused to some extent within the shallow design, collecting 61% through outlets 1 and 5 (Figure 3A). In contrast, 1 µm beads did not experience enough inertial lift force in the migration process even with the Dean flow assistance, and therefore remained unfocused in the deep design (~ 20% in each outlet, Figure 3B).

As demonstrated in Equation 1, the net lift force (F_L) depends very strongly on particle diameter, to the fourth order. This translates that at the same flow velocity and channel dimensions, smaller particles, in this case 1 µm, will focus to a lesser extent or not focus at all. Another relevant parameter is the inertial force ratio (R_f), introduced in Equation 5. Di Carlo [22] reported values of $R_f > 0.04$ to observe particle focusing. In our case, the R_f values for focused 10 µm and 4.5 µm particles in both devices into two streams along the channel side walls are > 0.04. Random migration of 1 µm particles was observed in the deep device ($R_f = 0.01$). In contrast, partial focusing of 1 µm particles was observed in the shallow device, where $R_f = 0.04$, closer to the cut-off value. With further reduction in channel depth, a complete focus of 1 µm particles might theoretically be possible.
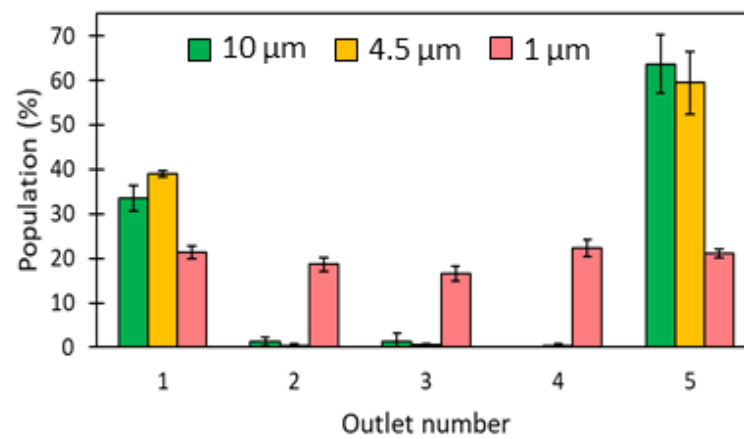
Figure 3. Fluorescent microscope photographs and focusing profiles of microparticles of different sizes (10, 4.5 and 1 µm) in (A) shallow (25 µm) channel design, and (B) deep (40 µm) channel design. Particle suspensions were separately pumped at 0.7 mL min^{-1} (n = 3).

4.3 Focusing profiles of cells

The deep design was tested with *E. coli* O157 cells (1-2 μm long, 0.5 μm wide [77]) at flow rates of 0.5 – 1 mL min^{-1}. In contrast to the larger 10 μm and 4.5 μm particles, *E. coli* remained unfocused (Figure S3-C, Supporting Information and Figure 4B). Due to the much smaller size of *E. coli* cells, they are more affected by the counter-rotating streamlines of a Dean vortex, and hence it is more difficult to align into equilibrium positions [50,51].

The focusing profile of *E. coli* in the shallow device differed from the deep design. The bacterial cells focused along the channel edges and exited at outlets 1 and 5 (recovery of *ca.* 89% at 0.7 mL min^{-1}, Figure S3-D, Supporting Information and Figure 4A). Interestingly, this shows that at the same Re_c = 56, the equilibrium positions of particles/cells ranging 10 – 1.5 μm were preferential along the channel side walls of the shallow device. With increasing flow velocities, the mixing effect became predominant, and a small migration of cells into exit 4 was observed (Figure S3-C, Supporting Information).

The difference between the *E. coli* focusing behaviors in the two designs (deep design: non-focused, and shallow design: focused) can be attributed to the suppression of the mixing effect of Dean vortex with lower channel depth [50,51]. Additionally, R_f values of *E. coli* (calculated using 1.5 μm diameter) were 0.09 and 0.02 for the shallow and deep designs, respectively (R_f > 0.04 to observe focusing [25]).

The two device designs were also subjected to 1:10 diluted horse blood cells (Figure 4). The RBCs are 6-8 μm in diameter [78], and should theoretically behave similarly to the 10 μm particles. Indeed, focusing of RBCs was observed along the channel edges and exited through outlets 1 and 5 in both devices. The performance of the shallow design was superior (89% recovery from outlets 1 and 5), whereas migration of RBCs into outlet 4 (20%) was seen in the deep device. Due to similar focusing behaviors of *E. coli* and RBCs in the shallow device (Figure 4A), it will not be possible to employ this design for separation of *E. coli* from blood matrix. However, the shallow design displayed a pre-concentration factor of x2.2 for *E. coli* cells, which could be useful to pre-enrich such bacteria, and those of similar sizes, in samples where narrow size-based separation (1-10 μm) is not needed. This pre-concentration factor could be increased by redesigning the side outlets to collect less volume. In addition, decreasing the channel depth to increase R_f can also be further investigated for

311 improved focusing performance. Such a high-throughput pre-concentration device
312 could be beneficial in bacteria concentration from urine samples for diagnostics of
313 urinary tract infections. Wang and Dandy [49] used an asymmetric serpentine device
314 for pre-concentration of cyanobacteria, which have a similar size (2 µm) to *E. coli*.
315 However, whilst demonstrating an excellent 98% bacterial recovery with 3.2x pre-
316 concentration factor, the significantly narrower dimensions of their device (20 µm
317 narrowest width x 10 µm depth) can be challenging for fabrication. In addition, this
318 device required a filter to prevent clogging, which would be likely to happen in such a
319 small cross-section.

320 In the deep device, however, RBCs and *E. coli* followed different focusing profiles.
321 Whilst RBCs preferentially migrated along the channel edges, *E. coli* behaved similarly
322 to 1 µm particles and mostly remained unfocused (Figure 4B). Together with previous
323 microparticle results, the deep device showed the potential for applications requiring
324 the separation of *E. coli* from larger microparticles and RBCs.
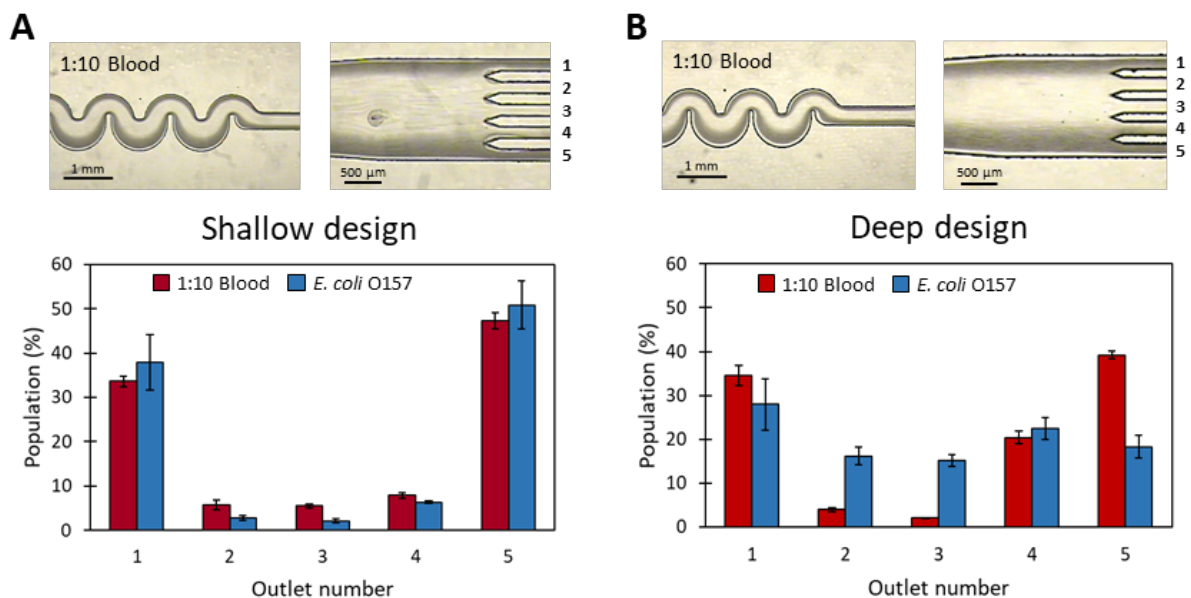
Figure 4. Microscope photographs and focusing profiles of 1:10 blood and *E. coli* O157 in (A) shallow (25 µm) channel design, and (B) deep (40 µm) channel design. Diluted blood and *E. coli* O157 suspensions were separately pumped at 0.7 mL min^{-1} (n = 3).

4.4 Separation of microparticles and *E. coli* O157

330 To study the separation performance of the deep design, a suspension of 10 µm and
331 4.5 µm fluorescent particles and *E. coli* was pumped through the device. The focusing
332 behaviour of mixed particles followed the same pattern as when they were separately
333 introduced. Results reported a successful recovery of 53% *E. coli* (outlets 2-4)

14

depleted from 91% of 10 µm beads and 94% of 4.5 µm beads, which were obtained
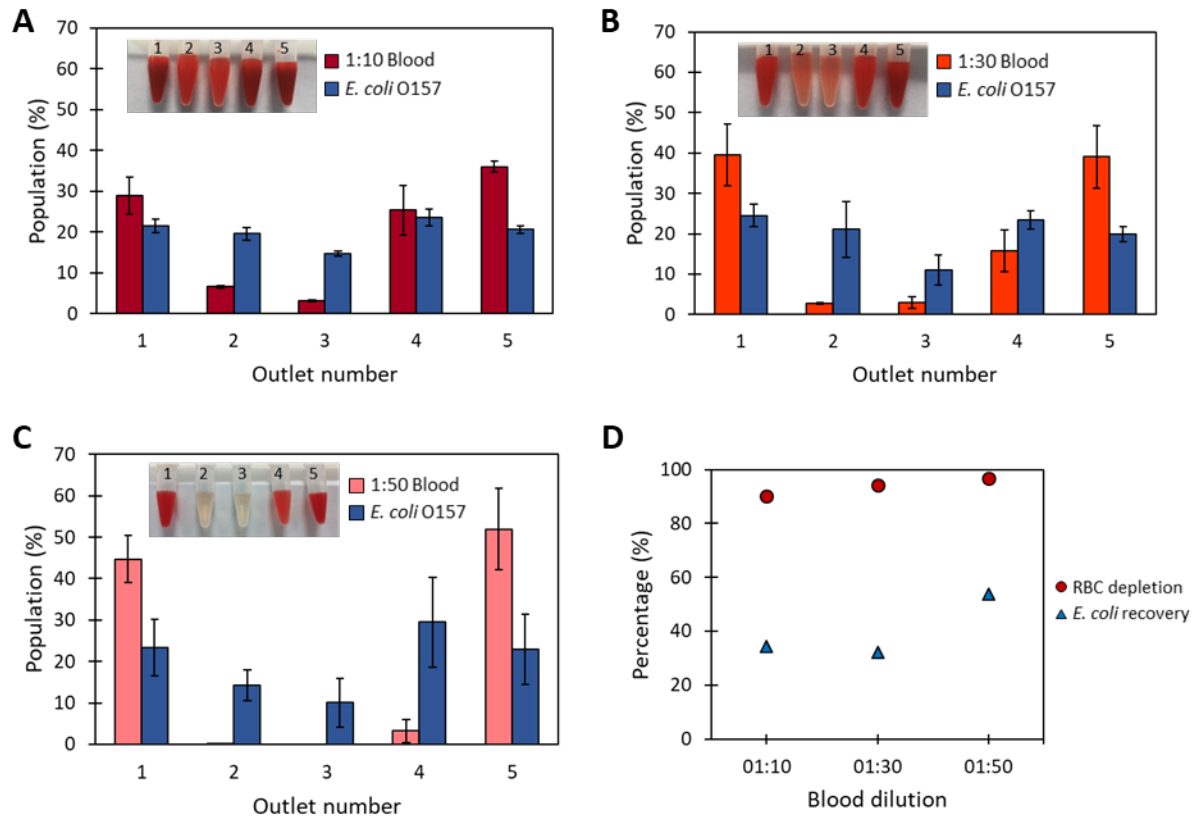through outlets 1 and 5 (Figure 5).
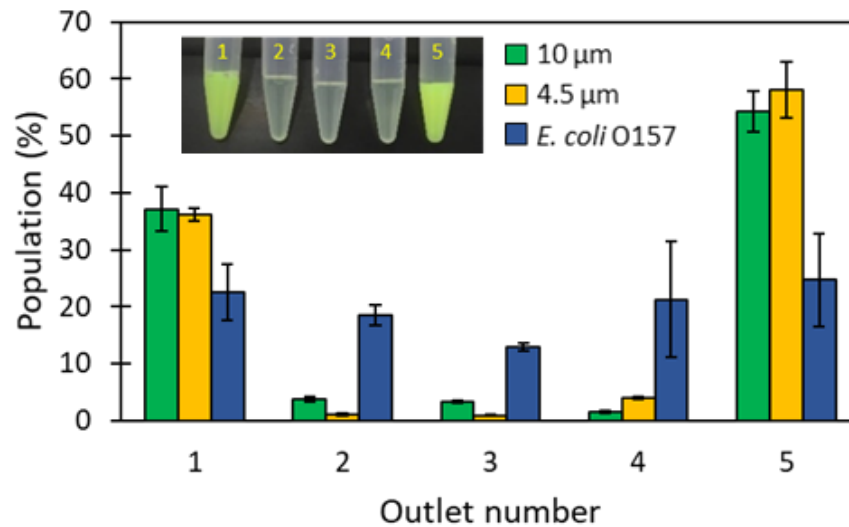
Figure 5. Inertial separation of a mixture of 10 µm (10^6 particles mL^{-1}) and 4.5 µm (10^7 particle mL^{-1}) fluorescent particles spiked with *E. coli* O157 (5×10^4 CFU mL^{-1}) on the deep (40 µm) channel design. The mixture was pumped at 0.7 mL min^{-1} (n = 3).

4.5 Separation of *E. coli* from blood samples

Although focusing of ≥ 8 µm particles in a single stream inside a symmetrical channel was reported [51], inertial blood separation has been performed in devices where focusing of RBCs took place in two streams along the channel edges [8,56]. When high concentrations of particles/cells (*i.e.* blood) flow through a channel, particle/cell ordering in a single narrow stream is more challenging due to steric crowding effects [79]. Instead, symmetric focusing in two streams along the channel side walls can be more easily achieved. Here, we exploited the inertial equilibrium positions of RBCs along the channel edges of the deep design for *E. coli* recovery from blood.

In order to reduce the steric effects associated with high blood cell concentration, blood was diluted 10x, 30x and 50x in PBST. Each dilution was spiked with similar *E. coli* O157 concentration of 5×10^4 CFU mL^{-1}. With increasing blood dilutions, higher separation of RBCs was obtained, thus improving the device efficiency. Recovery of 54% of *E. coli* depleted from 97% RBCs was achieved with a single pass of *E. coli*-spiked 1:50 blood (Figure 6).

Figure 6. Inertial separation of diluted horse blood solutions; (A) 1:10, (B) 1:30 and (C) 1:50 spiked with *E. coli* O157 on the deep (40 µm) channel design. (D) RBC depletion and *E. coli* recovery from different blood dilutions. The mixtures were pumped at 0.7 mL min^{-1} (n = 3).

To compare the performance of our device with other inertial devices reported for separation of bacteria from blood, blood dilutions were calculated as % hematocrit (Hct = volume percentage of red blood cells in blood). Human blood has an average of 45% Hct for men and 40% Hct for women [56], whist Hct from adult horse blood ranges between 31 to 50% [80].

A logical target is to separate a few bacteria from billions of RBCs from blood usually collected in vacutainer tubes (7-10 mL) in less than 10 min in order to provide time for downstream processes for molecular identification of pathogenic species [6]. Table 1 summarizes performances of inertial microfluidic devices for separation of bacteria from blood. The comparisons are based on operation in a single unit. Our device showed superior performance for RBCs depletion (97%) from less diluted blood (0.81% Hct) and higher throughput compared to the expanding straight channel device (88% RBCs depletion from 1:200 blood, 0.21% Hct) [8]. Although fewer *E. coli* cells were recovered, 54% efficiency was achieved after a single pass through the device.

16

373   Hou *et al.* [5] developed a spiral device for separating low concentrations of *E. coli*

374   (10-100 CFU mL^{-1}) from blood, employing a sheath fluid with x10 the sample flow.

375   Besides yielding >65% *E. coli* recovery from 1:3 diluted blood (~15% Hct) at 150 µL

376   min^{-1} flowrate, an array of 14 spiral devices would be required in order to process 7

377   mL of blood in 10 min. Parallelization for throughput improvement can be difficult to

378   achieve within the physical confines of the device compared to serpentine/straight

379   channels, especially when two pumps are required to control two independent inlet

380   flows. Faridi *et al.* [62] combined inertial microfluidics with a non-Newtonian

381   polyethylene oxide (PEO) sheath flow to recover 76% *E. coli* from whole blood with

382   the lowest generated waste volume. However, at such low flow rate of 0.5 µL min^{-1},

383   an impractically high number of single units would need to be run in parallel to process

384   7 mL of whole blood in a relevant time scale. Wu *et al.* [60] exploited a soft inertial

385   force device to separate *E. coli* mixed into human blood using a flow system in which

386   the diluted blood was sheathed with another flow, and subsequently deflected by an

387   'acting' flow. This system allowed for 300-fold bacteria enrichment (62% recovery)

388   from 1:10 human blood at 18 µL min^{-1}. However, the three-inlet system for the acting

389   flows requires a more complex fluidic control and generates large volumes of fluid to

390   be discarded, making it impractical to process 7 mL of whole blood in 10 min [6]. Using

391   the channel design reported herein, an arrangement of 50 separating channels in

392   parallel, fed from a single inlet, would have a potential maximum throughput of 7 mL

393   of whole blood in 10 min. Such a multiplexing array could be fabricated to sit within a

394   10 cm radius footprint.

395 **Table 1**. *Performance of different inertial devices for separation of RBC based on a single unit.*

Device	Asymmetric serpentine channel (this work)	Expanding straight channel [8]	Spiral channel [5]	Elasto-inertial straight channel [62]	Soft inertial-based channel [60]
Blood dilution	1:50	1:200	1:3	non-diluted	1:10
Hematocrit (%)	0.81*	0.21**	~15	42.5**	4.25**
RBC depletion (%)	97	88	-	-	98
E. coli recovery (%)	54	>80	>65	76	62
Flow rate (μL min^{-1})	700	200	150	0.5	18
Number of passes	1	2	1	1	1
Time required to process 7 mL of whole blood (h)	8.3	117	2.3	233	65
Total liquid volume needed to process 7 mL of whole blood (mL)	350	1400	231	91	798

396 *Calculated from an average of 40.5% horse hematocrit. **Calculated from an average of 42.5% human hematocrit.

397

398

In summary, we have explored, for the first time, glass serpentine devices for inertial focusing of small microparticles (1-10 μm) and cells (≤ 8 μm). Two different designs based on etched depth displayed different focusing behaviors and can be used for different applications. The ability of the shallow device to focus 1 μm particles and *E. coli* O157 (x2.2 preconcentrating factor) shows promise for bacteria pre-concentration applications. The feasibility of using the deep design for separation of *E. coli* from larger microparticles and RBCs (54% *E. coli* recovered from 97% depleted RBCs in 0.81% hematocrit) has been demonstrated. By parallelizing such serpentine channels, separation of bacteria from relevant volumes of 7 mL whole blood could potentially be achieved in 10 minutes. Such a platform would facilitate detection of pathogenic bacteria in blood with no or minimal culturing, thereby allowing faster diagnostics and timely assessment and treatment.

Acknowledgements

Conflict of interest

The authors have declared no conflict of interest.

Data Availability Statement

The data that support the findings of this study are available from the corresponding author upon reasonable request.

5 References

[1]   Rajapaksha, P., Elbourne, A., Gangadoo, S., Brown, R., Cozzolino, D., Chapman, J., Analyst 2019, 144, 396-411.
[2]   Varadi, L., Luo, J. L., Hibbs, D. E., Perry, J. D., Anderson, R. J., Orenga, S., Groundwater, P. W., Chem. Soc. Rev. 2017, 46, 4818-4832.
[3]   Abayasekara, L. M., Perera, J., Chandrasekharan, V., Gnanam, V. S., Udunuwara, N. A., Liyanage, D. S., Bulathsinhala, N. E., Adikary, S., Aluthmuhandiram, J. V. S.,

427   Thanaseelan, C. S., Tharmakulasingam, D. P., Karunakaran, T., Ilango, J., BMC Infect.
428   Dis. 2017, 17.

[4]   Yagupsky, P., Nolte, F. S., Clin. Microbiol. Rev. 1990, 3, 269-279.

[5]   Hou, H. W., Bhattacharyya, R. P., Hung, D. T., Han, J., Lab Chip 2015, 15, 2297-2307.

[6]   Pitt, W. G., Alizadeh, M., Husseini, G. A., McClellan, D. S., Buchanan, C. M., Bledsoe, C. G., Robison, R. A., Blanco, R., Roeder, B. L., Melville, M., Hunter, A. K., Biotechnol. Prog. 2016, 32, 823-839.

[7]   Al-Soud, W. A., Radstrom, P., J. Clin. Microbiol. 2001, 39, 485-493.

[8]   Mach, A. J., Di Carlo, D., Biotechnol. Bioeng. 2010, 107, 302-311.

[9]   Nivedita, N., Papautsky, I., Biomicrofluidics 2013, 7, 54101.

[10]   Tsutsui, H., Ho, C. M., Mech. Res. Commun. 2009, 36, 92-103.

[11]   Voldman, J., Annu. Rev. Biomed. Eng. 2006, 8, 425–454.

[12]   Ngamsom, B., Lopez-Martinez, M. J., Raymond, J. C., Broyer, P., Patel, P., Pamme, N., J. Microbiol. Methods 2016, 123, 79-86.

[13]   Zhou, J., Papautsky, I., Lab Chip 2013, 13, 1121-1132.

[14]   Amini, H., Lee, W., Di Carlo, D., Lab Chip 2014, 14, 2739-2761.

[15]   Zhang, J., Yan, S., Yuan, D., Alici, G., Nguyen, N. T., Warkiani, M. E., Li, W., Lab Chip 2016, 16, 10-34.

[16]   Tang, W., Jiang, D., Li, Z., Zhu, L., Shi, J., Yang, J., Xiang, N., Electrophoresis 2019, 40, 930-954.

[17]   Carey, T. R., Cotner, K. L., Li, B., Sohn, L. L., WIREs Nanomed. Nanobi. 2019, 11, e1529.

[18]   Gossett, D. R., Weaver, W. M., Mach, A. J., Hur, S. C., Tse, H. T., Lee, W., Amini, H., Di Carlo, D., Anal. Bioanal. Chem. 2010, 397, 3249-3267.

[19]   Warkiani, M. E., Khoo, B. L., Tan, D. S., Bhagat, A. A., Lim, W. T., Yap, Y. S., Lee, S. C., Soo, R. A., Han, J., Lim, C. T., Analyst 2014, 139, 3245-3255.

[20]   Warkiani, M. E., Tay, A. K., Guan, G., Han, J., Sci. Rep. 2015, 5, 11018.

[21]   Kuntaegowdanahalli, S. S., Bhagat, A. A., Kumar, G., Papautsky, I., Lab Chip 2009, 9, 2973-2980.

[22]   Di Carlo, D., Irimia, D., Tompkins, R. G., Toner, M., Proc. Natl. Acad. Sci. 2007, 104, 18892-18897.

[23]   Di Carlo, D., Edd, J. F., Irimia, D., Tompkins, R. G., Toner, M., Anal. Chem. 2008, 80, 2204-2211.

[24]   Jin, T., Yan, S., Zhang, J., Yuan, D., Huang, X. F., Li, W., Biomicrofluidics 2016, 10, 034104.

[25]   Di Carlo, D., Lab Chip 2009, 9, 3038-3046.

[26]   Sollier, E., Go, D. E., Che, J., Gossett, D. R., O'Byrne, S., Weaver, W. M., Kummer, N., Rettig, M., Goldman, J., Nickols, N., McCloskey, S., Kulkarni, R. P., Di Carlo, D., Lab Chip 2014, 14, 63-77.

[27]   Renier, C., Pao, E., Che, J., Liu, H. E., Lemaire, C. A., Matsumoto, M., Triboulet, M., Srivinas, S., Jeffrey, S. S., Rettig, M., Kulkarni, R. P., Di Carlo, D., Sollier-Christen, E., NPJ Precis. Oncol. 2017, 1.

[28]   Wu, Z., Chen, Y., Wang, M., Chung, A. J., Lab Chip 2016, 16, 532-542.

[29]   Seo, J., Lean, M. H., Kole, A., J. Chromatogr. A 2007, 1162, 126-131.

[30]   Bhagat, A. A., Kuntaegowdanahalli, S. S., Papautsky, I., Lab Chip 2008, 8, 1906-1914.

[31]   Seo, J., Lean, M. H., Kole, A., Appl. Phys. Lett. 2007, 91.

473 [32] Johnston, I. D., McDonnell, M. B., Tan, C. K. L., McCluskey, D. K., Davies, M. J., Tracey,
474   M. C., Microfluid. Nanofluid. 2014, 17, 509-518.
475 [33] Lee, J.-H., Lee, S.-K., Kim, J.-H., Park, J.-H., Sens. Actuators, A 2019, 286, 211-219.
476 [34] Yeh, P. Y., Dai, Z., Yang, X., Bergeron, M., Zhang, Z., Lin, M., Cao, X., Sens. Actuators,
477   B 2017, 252, 606-615.
478 [35] Syed, M. S., Rafeie, M., Vandamme, D., Asadnia, M., Henderson, R., Taylor, R. A.,
479   Warkiani, M. E., Bioresour. Technol. 2018, 252, 91-99.
480 [36] Jimenez, M., Miller, B., Bridle, H. L., Chem. Eng. Sci. 2017, 157, 247-254.
481 [37] Fuchs, B. B., Eatemadpour, S., Martel-Foley, J. M., Stott, S., Toner, M., Mylonakis, E.,
482   Front. Cell. Infect. Microbiol. 2019, 9, 27.
483 [38] Cruz, J., Graells, T., Wallden, M., Hjort, K., Lab Chip 2019, 19, 1257-1266.
484 [39] Xiang, N., Ni, Z., Biomed. Microdevices 2015, 17.
485 [40] Shen, S., Zhang, F., Wang, S., Wang, J., Long, D., Wang, D., Niu, Y., Sens. Actuators, B
486   2019, 287, 320-328.
487 [41] Wu, L., Guan, G., Hou, H. W., Bhagat, A. A., Han, J., Anal. Chem. 2012, 84, 9324-9331.
488 [42] Choi, K., Ryu, H., Siddle, K. J., Piantadosi, A., Freimark, L., Park, D. J., Sabeti, P., Han,
489   J., Anal. Chem. 2018, 90, 4657-4662.
490 [43] Chen, H., Sci. Rep. 2018, 8, 4042.
491 [44] Abdulla, A., Liu, W., Gholamipour-Shirazi, A., Sun, J., Ding, X., Anal. Chem. 2018, 90,
492   4397-4405.
493 [45] Gossett, D. R., Di Carlo, D., Anal. Chem. 2009, 81, 8459-8465.
494 [46] Oozeki, N., Ookawara, S., Ogawa, K., Löb, P., Hessel, V., AIChE J. 2009, 55, 24-34.
495 [47] Bayat, P., Rezai, P., Soft Matter 2018, 14, 5356-5363.
496 [48] Shiriny, A., Bayareh, M., Chem. Eng. Sci. 2021, 229, 116102.
497 [49] Wang, L., Dandy, D. S., Algal Res. 2017, 26, 481-489.
498 [50] Zhang, J., Alici, G., Li, W., Li, M., Nguyen, N. T., Microfluid. Nanofluid. 2014, 17, 305-
499   316.
500 [51] Zhang, J., Yan, S., Sluyter, R., Li, W., Alici, G., Nguyen, N. T., Sci. Rep. 2014, 4, 4527.
501 [52] Zhang, J., Yan, S., Alici, G., Nguyen, N.-T., Di Carlo, D., Li, W., RSC Adv. 2014, 4, 62076-
502   62085.
503 [53] Zhang, J., Yuan, D., Sluyter, R., Yan, S., Zhao, Q., Xia, H., Tan, S. H., Nguyen, N. T., Li,
504   W., IEEE Trans. Biomed. Circuits Syst. 2017, 11, 1422-1430.
505 [54] Ozbey, A., Karimzadehkhouei, M., Akgonul, S., Gozuacik, D., Kosar, A., Sci. Rep. 2016,
506   6, 38809.
507 [55] Ozbey, A., Karimzadehkhouei, M., Kocaturk, N. M., Bilir, S. E., Kutlu, O., Gozuacik, D.,
508   Kosar, A., Micro Nano Eng. 2019, 2, 53-63.
509 [56] Zhang, J., Yan, S., Li, W., Alici, G., Nguyen, N.-T., RSC Adv. 2014, 4, 33149.
510 [57] Li, L., Wu, P., Luo, Z., Wang, L., Ding, W., Wu, T., Chen, J., He, J., He, Y., Wang, H.,
511   Chen, Y., Li, G., Li, Z., He, L., ACS Sens. 2019, 4, 1299-1305.
512 [58] Rafeie, M., Zhang, J., Asadnia, M., Li, W., Warkiani, M. E., Lab Chip 2016, 16, 2791-
513   2802.
514 [59] Jiang, F., Xiang, N., Ni, Z., Electrophoresis 2020, 41, 2136-2143.
515 [60] Wu, Z., Willing, B., Bjerketorp, J., Jansson, J. K., Hjort, K., Lab Chip 2009, 9, 1193-
516   1199.
517 [61] Zelenin, S., Ardabili, S., Brismar, H., Hansson, J., Ramachandraiah, H., Russom, A.,
518   Biotechnol. Lett. 2015, 37, 825–830.

519 [62] Faridi, M. A., Ramachandraiah, H., Banerjee, I., Ardabili, S., Zelenin, S., Russom, A., J.
520 Nanobiotechnol. 2017, 15, 1-9.
521 [63] Lu, X., Chow, J. J. M., Koo, S. H., Tan, T. Y., Jiang, B., Ai, Y., Anal. Chem. 2020, 92,
522 15579-15586.
523 [64] Ramachandraiah, H., Svahn, H. A., Russom, A., RSC Adv. 2017, 7, 29505-29514.
524 [65] Zhang, J., Chintalaramulu, N., Vadivelu, R., An, H., Yuan, D., Jin, J., Ooi, C. H., Cock, I.
525 E., Li, W., Nguyen, N. T., Anal. Chem. 2020, 92, 11558-11564.
526 [66] Ren, H., Zhu, Z., Xiang, N., Wang, H., Zheng, T., An, H., Nguyen, N.-T., Zhang, J., Sens.
527 Actuators, B 2021, 337, 129758.
528 [67] Huang, D., Man, J., Jiang, D., Zhao, J., Xiang, N., Electrophoresis 2020, 41, 2166-2187.
529 [68] Chung, A. J., Biochip J. 2019, 13, 53-63.
530 [69] Martel, J. M., Toner, M., Sci. Rep. 2013, 3.
531 [70] Asmolov, E. S., J. Fluid Mech. 1999, 381, 63-87.
532 [71] Di Carlo, D., Edd, J. F., Humphry, K. J., Stone, H. A., Toner, M., Phys. Rev. Lett. 2009,
533 102, 094503.
534 [72] Gossett, D. R., Tse, H. T., Dudani, J. S., Goda, K., Woods, T. A., Graves, S. W., Di Carlo,
535 D., Small 2012, 8, 2757-2764.
536 [73] Zhang, J., Yuan, D., Zhao, Q., Teo, A. J. T., Yan, S., Ooi, C. H., Li, W., Nguyen, N. T.,
537 Anal. Chem. 2019, 91, 4077-4084.
538 [74] Scheuble, N., Iles, A., Wootton, R. C. R., Windhab, E. J., Fischer, P., Elvira, K. S., Anal.
539 Chem. 2017, 89, 9116-9123.
540 [75] McCreedy, T., Anal. Chim. Acta 2001, 427, 39-43.
541 [76] Özbey, A., Karimzadehkhouei, M., Alijani, H., Koşar, A., Fluids 2018, 3, 57.
542 [77] Riley, M., *Size Limits of Very Small Microorganisms: Proceedings of a Workshop*,
543 National Academy Press 1999, p. 21-26.
544 [78] Ward, J. M., Cherian, S., Linden, M. A., S.M.D.a.K.S.M. Piper M. Treuting (Ed.),
545 *Comparative Anatomy and Histology (Second Edition)* 2018, p. 365-401.
546 [79] Martel, J. M., Toner, M., Annu. Rev. Biomed. Eng. 2014, 16, 371-396.
547 [80] Southwood, L. L., *Practical Guide to Equine Colic, First Edition*, John Wiley & Sons,
548 Inc. 2013, p. 339-342.

Supporting information

549

550 **Supporting information file:** Inertial microfluidic devices; Effect of flow rates on
551 inertial focusing of particles and *E. coli* O157; Estimated values of F_L/F_D scaling factor
552 and modified particle-blockage ratio.

Supporting Information

Inertial focusing of microparticles, bacteria and blood in serpentine glass channels

Pablo Rodriguez-Mateos,[1] Bongkot Ngamsom,[1] Charlotte E. Dyer,[2] Alexander Iles,[1] Nicole Pamme[1*]

[1] Department of Chemistry and Biochemistry, University of Hull, UK.

[2] Department of Biomedical Sciences, University of Hull, UK.

*Correspondence should be addressed to the following author(s):

Prof. Nicole Pamme

Department of Chemistry and Biochemistry, Faculty of Science and Engineering

University of Hull

Cottingham Road, Hull, HU6 7RX, UK
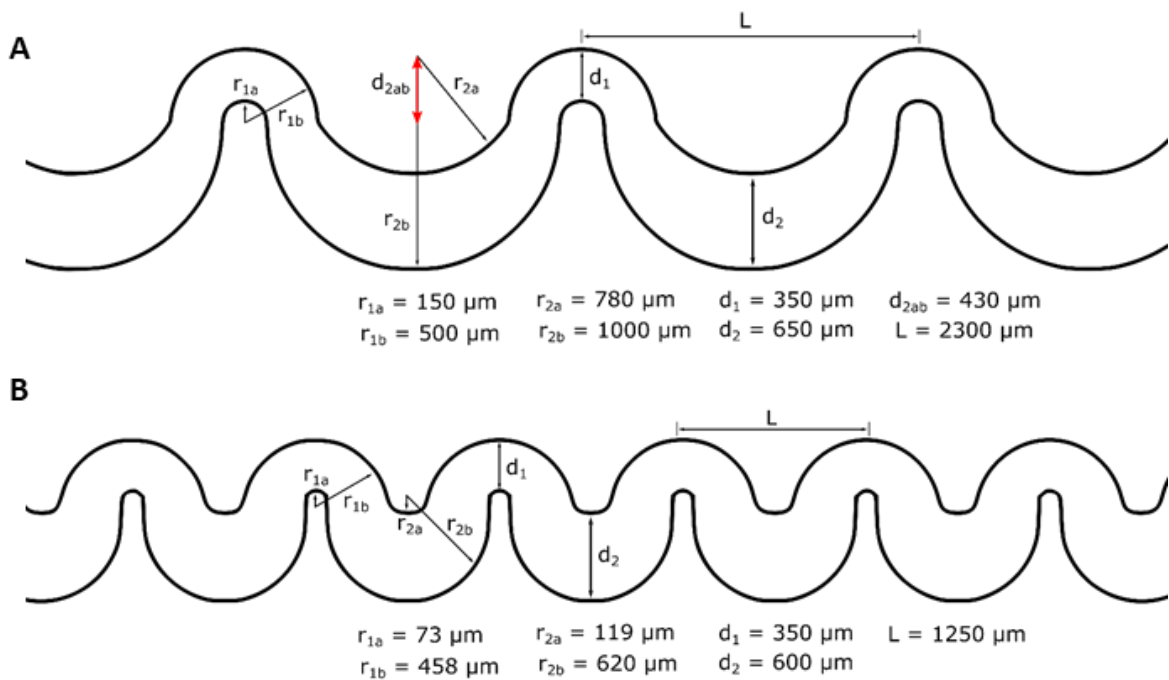
n.pamme@hull.ac.uk

Table of contents

S1 Inertial microfluidic devices

Two designs were employed, etched at two different depths from the same photomask, and referred to as 'shallow design' (25-µm depth) and 'deep design' (40-µm depth). The channel pathway for both devices was laid out asymmetrically, with a series of 49 alternating narrow and wide turns over a distance of 30 mm. The radii of curvature between the narrow and wide turns, $(r_{1b}/r_{1a})/(r_{2b}/r_{2a})$, in our device are more similar compared to those used in asymmetric serpentine devices reported by Di Carlo *et al*. [1,2]. This also results in our device having a distance between two narrow turns (L) almost half as Di Carlo's (Figure S1, Table S1).

A

$r_{1a} = 150$ µm $r_{2a} = 780$ µm $d_1 = 350$ µm $d_{2ab} = 430$ µm
$r_{1b} = 500$ µm $r_{2b} = 1000$ µm $d_2 = 650$ µm   L = 2300 µm

B

$r_{1a} = 73$ µm $r_{2a} = 119$ µm $d_1 = 350$ µm   L = 1250 µm
$r_{1b} = 458$ µm $r_{2b} = 620$ µm $d_2 = 600$ µm

Figure S1. Comparison of dimensinos and radii of curvature between Di Carlo's device (A), and ours (B), etched at two depths.

**Table S1.** Comparison of radii of curvature and turn ratios between Di Carlo's device and ours.

	Our device	Di Carlo's [2]
Largest radius in narrow turn, r_{1b} (µm)	458	500
Smallest radius in narrow turn, r_{1a} (µm)	73	150
r_{1b}/r_{1a} (narrow turn)	6.3	3.3
Largest radius in wide turn, r_{2b} (µm)	620	1000
Smallest radius in wide turn, r_{2a} (µm)	119	780
r_{2b}/r_{2a} (wide turn)	5.2	1.3
$(r_{1b}/r_{1a}) / (r_{2b}/r_{2a})$	1.2	2.6
Distance between two narrow turns, L (µm)	1250	2300

The microfluidic glass channels were etched with dilute hydrofluoric acid using a photomask of width m. Due to isotropic etching, the final channel width at the bottom will be the photomask width m, but the final channel width at the top (w) will be wider, and can be determined according to $w = (2d) + m$, where d is the channel depth. This means that for a channel etched at 40 µm deep, the final top width will be 80 µm wider than the photomask/bottom width (40 µm on each side). This results in curved sidewalls (Figure S2).
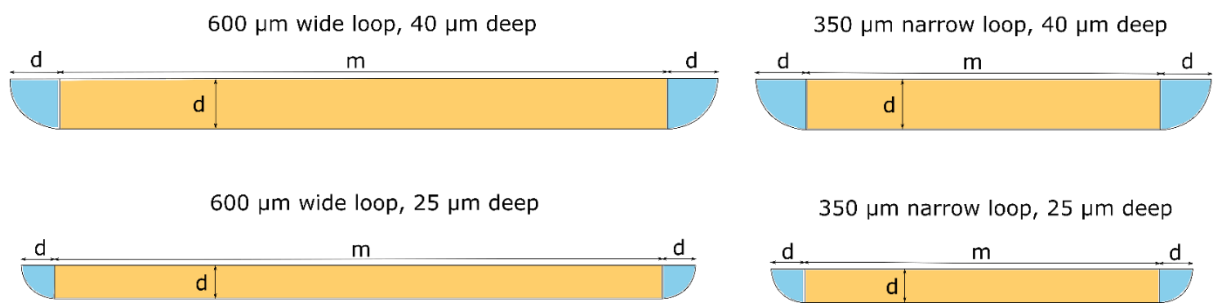
Figure S2. Cross-sectional areas of the narrow and wide turns in both shallow and deep devices after isotropic hydrofluoric acid etching of glass.

S2 Effect of flow rates on inertial focusing of particles and *E. coli* O157

54 Different flow rates were investigated for focusing of particles and *E. coli* O157. For

55 the deep design, increasing flowrate resulted in better depletion of 10 µm particles,

56 but worsened the focusing for 4.5 µm particles (Figure S3 A, B). Flow rate had no

57 significant effect on the focussing of the *E. coli* in the deep design (Figure S3 C). For

58 the shallow device, 0.7 mL min^{-1} flow rate resulted in better focusing of *E. coli* (Figure

59 S3 D).
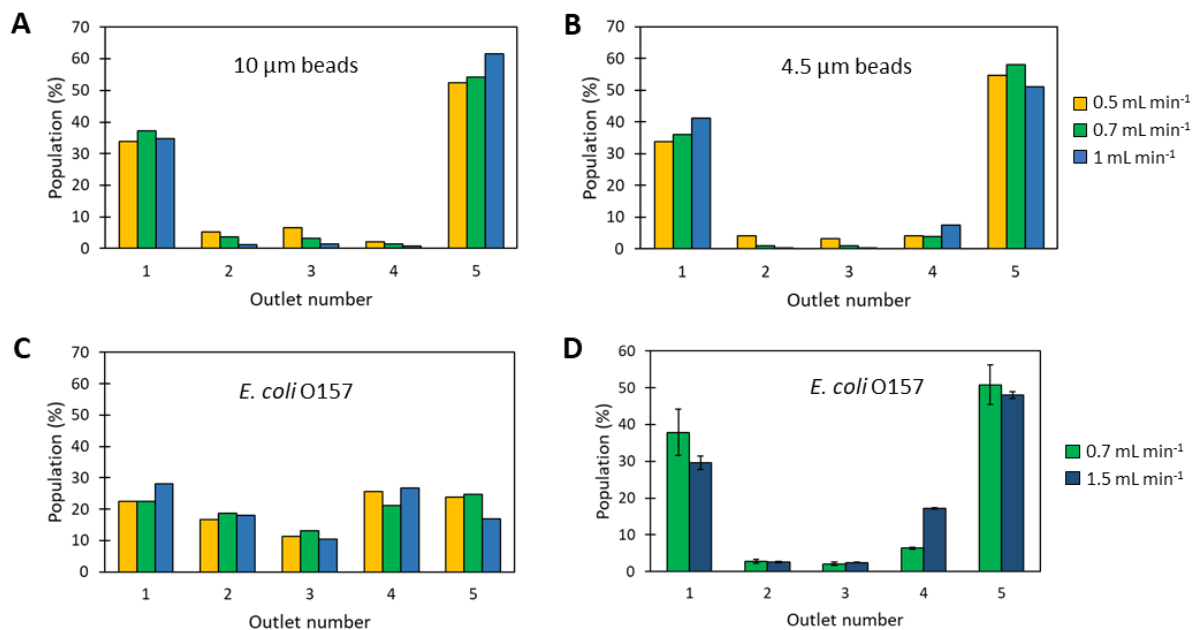
60

61 **Figure S3.** Focusing profiles of (A) 10 µm, (B) 4.5 µm and (C) *E. coli* at 0.5, 0.7 and 1

62 mL min^{-1} on the deep design. (D) Focusing profiles of *E. coli* at 0.7 and 1.5 mL min^{-1}

63 on the shallow design.

S3 Estimated values of F_L/F_D scaling factor and modified particle-blockage ratio

Table S2. Comparison of F_L/F_D scaling factor (δ) and modified particle-blockage ratio (MPBR) [3] of different particle sizes in both devices operating at 0.7 mL min^{-1}.

	Deep device (Re_c = 56)			Shallow device (Re_c = 52)		
Particle size (µm)	10	8*	4.5	10	8*	4.5
δ	0.10	0.08	0.04	0.22	0.18	0.10
MPBR	0.19	0.16	0.09	0.31	0.25	0.14

*Approximated particle size of red blood cells.

References

[1]   Di Carlo, D., Irimia, D., Tompkins, R. G., Toner, M., Proc. Natl. Acad. Sci. 2007, 104, 18892-18897.

[2]   Di Carlo, D., Edd, J. F., Irimia, D., Tompkins, R. G., Toner, M., Anal. Chem. 2008, 80, 2204-2211.

[3]   Zhang, J., Yuan, D., Zhao, Q., Teo, A. J. T., Yan, S., Ooi, C. H., Li, W., Nguyen, N. T., Anal. Chem. 2019, 91, 4077-4084.